

Rethinking RGB-D Salient Object Detection: Models, Datasets, and Large-Scale Benchmarks

Deng-Ping Fan, Zheng Lin, Jia-Xing Zhao, Yun Liu,
Zhao Zhang, Qibin Hou, Menglong Zhu, and Ming-Ming Cheng

Abstract—The use of RGB-D information for salient object detection has been explored in recent years. However, relatively few efforts have been spent in modeling salient object detection over real-world human activity scenes with RGB-D. In this work, we fill the gap by making the following contributions to RGB-D salient object detection. First, we carefully collect a new salient person (SIP) dataset, which consists of 1K high-resolution images that cover diverse real-world scenes from various viewpoints, poses, occlusion, illumination, and background. Second, we conduct a large-scale and so far the most comprehensive benchmark comparing contemporary methods, which has long been missing in the area and can serve as a baseline for future research. We systematically summarized 31 popular models, evaluated 17 state-of-the-art methods over seven datasets with totally about 91K images. Third, we propose a simple baseline architecture, called Deep Depth-Depurator Network (D³Net). It consists of a depth depurator unit and a feature learning module, performing initial low-quality depth map filtering and cross-modal feature learning respectively. These components form a nested structure and are elaborately designed to be learned jointly. D³Net exceeds the performance of any prior contenders across five metrics considered, thus serves as a strong baseline to advance the research frontier. We also demonstrate that D³Net can be used to efficiently extract salient person masks from the real scenes, enabling effective background changed book cover application with 20 fps on a single GPU. All the saliency maps, our new SIP dataset, baseline model, and evaluation tools are made publicly available at <https://github.com/DengPingFan/D3NetBenchmark>.

Index Terms—Salient Object Detection, RGB-D Saliency, Benchmark, Dataset.

I. INTRODUCTION

HOW to take beautiful photos has become one of the most important competition points among mobile phone manufacturers. Salient object detection (SOD) methods [1]–[17] have been widely used in taking perfect portraits by automatically adding large aperture and other enhancement effects. While existing SOD methods [18]–[34] have achieved remarkable success, most of them only rely on RGB images and ignore the important depth information, which is widely available in modern smart phones (*e.g.*, iPhone X, Huawei Mate10, and Samsung Galaxy S10). Fully utilizing RGB-D information for SOD detection has recently attracted great research attention [35]–[50].

On of primary goals of existing intelligent phone is understanding the humans in visual scenes. It involves several

D.-P. Fan, Z. Lin, J.-X. Zhao, Y. Liu, Z. Zhang, Q. Hou, and M.-M. Cheng are with the CS, Nankai University (Email: dengpingfan@mail.nankai.edu.cn).

M. Zhu is with the Google AI, USA.

M.-M. Cheng is the corresponding author (Email: cmm@nankai.edu.cn).

Manuscript received July xx, 2019; revised xxxx xx, xxxx.

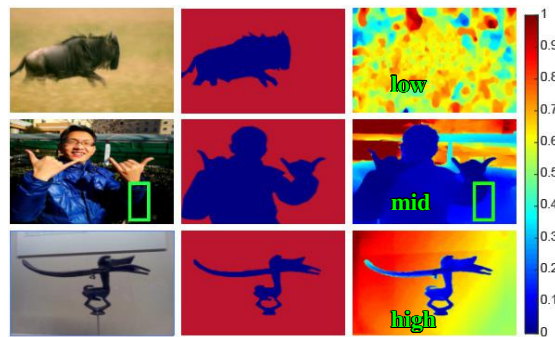


Fig. 1. Left to right: input image, ground-truth, and the corresponding depth map. The quality of the depth map from low (1st row), mid (2nd row) to high (last row). As shown in the 2nd row, it is difficult to recognize the boundary of the human’s arm in the boundary box region. However, it is clearly visible in the depth map. The high-quality depth maps will benefit the RGB-D based salient object detection task. These three examples are from NJU2K [36], our SIP and NLPR [38] datasets respectively.

typical perceptual tasks including detection, *i.e.*, localizing different persons at a coarse, bounding-box level, instance segmentation, *i.e.*, annotating each pixel of each person uniquely, *i.e.*, decomposing persons into their semantic categories [51]. To this end, intelligent solutions, such as saliency detecting and depth information utilizing, have caught considerable researchers attention.

However, existing RGB-D based SOD methods are mostly tested on RGB-D images taken by Kinect [52], light field camera [53] or estimated by optical flow [54], which have different characteristics from the *actual* smart phone cameras. Since human is the key subject of the smart phone, thus a human-oriented RGB-D dataset reflecting the realistic in the wild will be more important for mobile manufacturers. Despite the effort of some authors [36], [38] to augment their scenes with additional objects, a human-centered RGB-D dataset for salient object detection does not yet exist.

Furthermore, although depth map provides important complementary information for identifying salient objects. Sometimes the initial low-quality depth maps may cause wrong detections [55]. While existing RGB-D based SOD models typically fuse RGB and depth features by different strategies [50], such explicitly/automatically discard the initial low-quality depth map models are missing for RGB-D saliency modeling. We believe such models are highly desired to drive this field forward.

Besides the limitations of current RGB-D dataset and RGB-

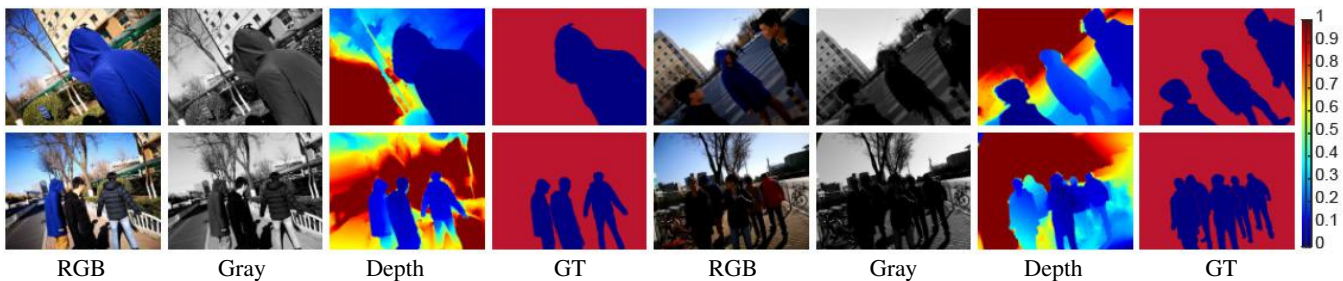


Fig. 2. Examples of images, depth maps and annotations in our *SIP* dataset with different number of salient objects, object size, object position, scene complexity, and lighting conditions. Note that the “RGB” and “Gray” images are captured by two different monocular cameras with small distance. Thus, the “Gray” image is slightly different from the grayscale image obtained from colorful (RGB) image. Our *SIP* dataset provides a potential direction such as depth estimating from the “RGB” and “Gray” image.

D model, most RGB-D based benchmarks also suffer from common limitations including:

- **Sufficiency.** Only limited datasets (1~4) are benchmarked in recent papers [38], [56] (Table II). The generalization ability of the models cannot be properly accessed with such a small number of datasets in the benchmark.
- **Completeness.** F-measure [57], MAE, and PR are the three widely-used metrics in existing works. However, as suggested by [58], [59], these metrics are essentially per-pixel. It is difficult to draw a thorough and reliable conclusions from quantitative evaluations [60].
- **Fairness.** Some works [48], [50], [61] use the *same* F-measure metric, while they do not explicitly describe which statistic (*e.g.*, mean or max) they used, easily resulting in unfair comparison and inconsistent performance. Meanwhile, the different threshold strategies in F-measure (*e.g.*, 255 varied thresholds [50], [61], [62], adaptive saliency threshold [38], [40], and self-adaptive threshold [42]) will result in different performance. Fairly comparing RGB-D based SOD models by extensively evaluating them with same metrics on standard benchmarks is highly desired.

A. Contribution

To solve the above mentioned problem, we make three distinct contributions.

- We built a new **Salient Person (SIP)** dataset (see Fig. 2). It consists of 1K accurately annotated high-resolution images which are designed to contain multiple salient persons per image. It’s worth mentioning that the depth maps are captured by the real smart phone. We believe such dataset is highly desired and drives RGB-D model to work in the mobile devices. Besides, the dataset is carefully selected to cover diverse scenes, various challenging situations (*e.g.*, occlusion, appearance change), and elaborately annotated with pixel-level ground truth (GT). Another discriminative feature of our *SIP* dataset is the availability of both RGB and Gray images captured by binocular camera, benefiting broader potential research directions, for example, stereo matching, depth estimating and human-centered detection, *etc.*
- With the proposed *SIP* dataset and existing six RGB-D datasets [36]–[38], [63]–[65], we provide a more

comprehensive summarization of 31 classical RGB-D salient object detection models and present the largest-scale (~91K images) fair evaluation of 17 state-of-the-art algorithms [36]–[46], [48], [55], [66]–[68], making it a good all-around RGB-D benchmark. To further promote the development of this field, we additionally provide an online evaluation platform with the preserved test set.

- Technically, we propose a simple baseline model called Deep Depth-Depurator Network (**D³Net**), which learns to automatically discard the initial low-quality depth map using a novel depth depurator unit (DDU). Together with a feature learning module, our D³Net can predict the salient object accurately. Extensive experiments in this study show that our D³Net remarkably outperforms prior work on many challenge datasets. Such a general framework design helps to learn the cross-modality features from RGB image and depth map and motivates potential model designing effectively.

Our contributions offer a systematic benchmark suite with the basic tools for a comprehensive assessment, offering a deep insight into the task of RGB-D based modeling and encouraging future research towards this direction.

B. Organization

In Section II, we first review previous datasets for RGB-D salient object detection and representative RGB-D models related to SOD. Then, we present details of our proposed salient person dataset *SIP* in Section III. In Section IV, we describe our D³Net model for RGB-D salient object detection by filtering the low-quality depth map and learning the cross-modal feature explicitly.

In Section V, we provide both quantitative and qualitative experimental analysis of the proposed algorithm. Specifically, in Section V-A, we offer more details on our experimental settings, including benchmarked models, datasets and runtime. In Section V-B, five metrics such as E-measure [59], S-measure [58], MAE, PR Curve, and F-measure are described in detail. In Section V-C, the mean statistic over six datasets, namely STEREO [63], LFS [65], DES [37], NLPR [38], NJU2K [36], SSD [64], and *SIP (Ours)* with the comparison to 17 state-of-the-art RGB-D SOD models clearly demonstrate the robustness and efficiency of our model. Further, in Section V-D, we provide the performance comparison between

TABLE I

COMPARISON OF CURRENT RGB-D DATASETS IN TERMS OF YEAR (**YEAR**), PUBLICATION (**PUB.**), DATASET SIZE (**DS.**), NUMBER OF OBJECTS IN THE IMAGES (**#OBJ.**), TYPE OF SCENE (**TYPES.**), DEPTH SENSOR (**SENSOR.**), DEPTH QUALITY (**DQ.**, *e.g.*, HIGH-QUALITY DEPTH MAP SUFFERS FROM LESS RANDOM NOISE. SEE LAST ROW IN FIG. 1), ANNOTATION QUALITY (**AQ.**, SEE FIG. 11), WHETHER PROVIDE GRAY IMAGE FROM MONOCULAR CAMERA (**GL.**), CENTER BIAS (**CB.**, SEE FIG. 3 (A)-(B)), AND RESOLUTION (IN PIXEL). H & W DENOTE THE HEIGHT AND WITH OF THE IMAGE, RESPECTIVELY.

No.	Dataset	Year	Pub.	DS.	#Obj.	Types.	Sensor.	DQ.	AQ.	GL.	CB.	Resolution (H×W)
1	<i>STERE</i> [63]	2012	CVPR	1K	~one	internet	Stereo camera+sift flow [54]		High	No	High	[251~1200]×[222~900]
2	<i>GIT</i> [35]	2013	BMVC	0.08K	multiple	home environment	Microsoft Kinect [52]		High	No	Low	640 × 480
3	<i>LFSD</i> [65]	2014	CVPR	0.1K	one	60 indoor/40 outdoor	Lytro Illum camera [53]		High	No	High	360 × 360
4	<i>DES</i> [37]	2014	ICIMCS	0.135K	one	135 indoor	Microsoft Kinect [52]	High		No	High	640 × 480
5	<i>NLPR</i> [38]	2014	ECCV	1K	multiple	indoor/outdoor	Microsoft Kinect [52]	High		No	High	640 × 480, 480 × 640
6	<i>NJU2K</i> [36]	2014	ICIP	1.985K	~one	3D movie/internet/photo	FujiW3 camera+optical flow [69]		High	No	High	[231~1213]×[274~828]
7	<i>SSD</i> [64]	2017	ICCVW	0.08K	multiple	three stereo movies	Sun's optical flow [69]			No	Low	960 × 1080
8	<i>SIP (Ours)</i>	2019		1K	multiple	person in the wild	Huawei Mate10	High	High	Yes	Low	992×744

traditional and deep models. We also provide deeper insights into the experimental results and give some possible direction for future work. In Section V-E, we provide visualizations of the results and report saliency maps generated on various of challenging scenes. In Section VI, we demonstrate an interesting yet realistic use scenario of D³Net in a background changed book cover application. To better understand the contributions of different component of the proposed D³Net, in Section VII, we implement several variants of our algorithm to conduct detailed ablative studies. All in all, the extensive experimental results clearly demonstrate that our D³Net model exceeds the performance of any prior competitors across 5 different metrics. In Section VII-A, we discuss the limitation of this work. Finally, Section VIII concludes the paper.

II. RELATED WORKS

A. RGB-D Datasets

Over the past few years, several RGB-D datasets have been constructed for SOD. Some statistics of these datasets are shown in Table I. More specifically, *STERE* [63] dataset is the first stereoscopic photo collection in this field. *GIT* [35], *LFSD* [65] and *DES* [65] are three small size datasets. The *GIT* and *LFSD* datasets are designed for their specific purposes, *e.g.*, saliency-based segmentation of generic objects, and saliency detection on the light field, while *DES* has 135 indoor images captured by Microsoft Kinect [52]. Although above datasets advanced the field to various degrees, they are severely restricted by the small scale or low resolution. To overcome this barriers, Peng *et al.* created *NLPR* [38], a large scale of RGB-D dataset with the resolution of 640×480. Later, Ju *et al.* built *NJU2K* [36] that has become one of the most popular RGB-D datasets. A recent *SSD* [64] dataset partially remedied the resolution restriction of *NLPR* and *NJU2K*. But its image scale are quite limited as it contains only 80 sample images. A common limitation, however, of existing RGB-D dataset is that they do not capture the depth map in the real smart phone and are not suitable for reflecting the real environment settings (*e.g.*, lighting conditions or distance to the object,*etc.*).

Compared to previous datasets, the proposed *SIP* dataset has three fundamental differences: (1) It includes 1,000 images with many challenging situations [70] (*e.g.*, dark background, occlusion, appearance change, and out-of-view, *etc.*) from

various outdoor scenarios. (2) The RGB, Gray image, and the estimated depth map are captured by the smart phone with a dual camera. Due to the predominant application of SOD to human subjects on mobile phones, we focus on capturing the person, and thus, for the first time, emphasize the salient person in the real-world scenes. (3) A detailed quantitative analysis is presented about the quality of the dataset (*e.g.*, center bias, object size, *etc.*), which are not carefully investigated in previous RGB-D based studies.

B. RGB-D Models

Traditional models rely heavily on hand-crafted features (*e.g.*, contrast [37], [38], [74], [76], shape [35]). By embedding the classical principles (*e.g.*, spatial bias [37], center-dark channel [45], 3D [78], background [39], [46]), difference of Gaussian [36], region classification [62], SVM [44], [74], graph knowledge [55], cellular automata [41], and markov random field [39], [76], they show that these features can lead to decent performance. They also explored the way of integrating RGB and depth feature via various combination, such as angular density [40], random forest regressor [44], [62], and minimum barrier distance [78]. More details are shown in Table II.

To overcome the limited expression ability of hand-crafted features, recent works [42], [43], [47], [48], [50], [61], [77], [79], [81]–[83] propose to introduce CNNs to infer salient object from RGB-D data. BED [77] and DF [43] are the two pioneering works that introduce deep learning technology in RGB-D based SOD task. More recently, Huang *et al.* develop a more efficient end-to-end model [79] with a modified loss function. To address the shortage of training data, Zhu *et al.* [47] present a robust prior model with guided depth-enhanced module for SOD. Besides, Chen *et al.* develop a series of novel approaches, such as hidden structure transfer [42], complementarity fusion module [48], attention-aware component [81], [83], and dilated convolutional [82] in this field. Nevertheless, these works, to our best knowledge, are dedicated to extracting depth feature/information via various strategies.

We argue that not all information in the depth map is informative for SOD, and the low-quality depth map often bring much noise (*e.g.*, 1st row in Fig. 1). Instead, we design a simple baseline model (D³Net), which is equipped with a

TABLE II

SUMMARIZATION OF 31 CLASSICAL RGB-D BASED SOD ALGORITHMS AND THE PROPOSED BASELINE (D³NET). **TRAIN/VAL SET. (#)** = TRAINING OR VALIDATION SET: *NLR* = *NLPR* [38], *NJU* = *NJU2K* [36], *O* = *MSRA10K* [71] + *DUTS* [72]. **BASIC:** 4PRIORS = 4 PRIORS, *e.g.*, REGION, BACKGROUND, DEPTH, AND SURFACE ORIENTATION PRIOR. **IPT** = INITIALIZATION PARAMETERS TRANSFER. **LGBS PRIORS** = LOCAL CONTRAST, GLOBAL CONTRAST, BACKGROUND, AND SPATIAL PRIOR. **RFR** [73] = RANDOM FOREST REGRESSOR. **MCFM** = MULTI-CONSTRAINT FEATURE MATCHING. **CLP** = CROSS LABEL PROPAGATION. **TYPE:** T = TRADITIONAL. **D** = DEEP LEARNING. **SP.** = SUPERPIXEL: WHETHER SUPERPIXEL ALGORITHM IS USED? **E-MEASURE:** THE RANGE OF SCORES OVER THE 7 DATASETS IN TABLE V. EVALUATION TOOLS: [HTTPS://GITHUB.COM/DENGPINGFAN/E-MEASURE](https://github.com/DengPingFan/E-Measure).

No.	Model	Year	Pub.	Train/Val Set. (#)	Test (#)	Basic	Type	SP.	E-measure [†] [59]
1	LS [35]	2013	BMVC		One	Markov Random Field	T	✓	
2	RC [74]	2013	BMVC		One	Region Contrast, SVM [75]	T		
3	LHM [38]	2014	ECCV		One	Multi-Context Contrast	T	✓	0.653~0.771
4	DESM [37]	2014	ICIMCS		One	Color/Depth Contrast, Spatial Bias Prior	T		0.770~0.868
5	ACSD [36]	2014	ICIP		One	Difference of Gaussian	T	✓	0.780~0.850
6	SRDS [76]	2014	DSP		One	Weighted Color Contrast	T		
7	GP [39]	2015	CVPRW		Two	Markov Random Field, 4Priors	T	✓	0.670~0.824
8	PRC [62]	2016	Access		Two	Region Classification, RFR	T		
9	LBE [40]	2016	CVPR		Two	Angular Density Component	T	✓	0.736~0.890
10	DCMC [55]	2016	SPL		Two	Depth Confidence, Compactness, Graph	T	✓	0.743~0.856
11	SE [41]	2016	ICME		Two	Cellular Automata	T	✓	0.771~0.856
12	MCLP [66]	2017	Cybernetic		Two	Addition, Deletion and Iteration Scheme	T	✓	
13	TPF [64]	2017	ICCVW		Four	Cellular Automata, Optical Flow	T	✓	
14	CDCP [45]	2017	ICCVW		Two	Center-dark Channel Prior	T	✓	0.700~0.820
15	DF [43]	2017	TIP	<i>NLR</i> (0.75K) + <i>NJU</i> (1.0K)	Three	Laplacian Propagation, LGBS Priors	D	✓	0.759~0.880
16	BED [77]	2017	ICCVW	<i>NLR</i> (0.80K) + <i>NJU</i> (1.6K)	Two	Background Enclosure Distribution	D	✓	
17	MDSF [44]	2017	TIP	<i>NLR</i> (0.50K) + <i>NJU</i> (0.5K)	Two	SVM [75], RFR, Ultrametric Contour Map	T		0.779~0.885
18	MFF [78]	2017	SPL		One	Minimum Barrier Distance, 3D prior	T		
19	Review [56]	2018	TCSVT		Two		T		
20	HSCS [67]	2018	TMM		Two	Hierarchical Sparsity, Energy Function	T	✓	
21	ICS [68]	2018	TIP		One	MCFM, CLP	T	✓	
22	CDB [46]	2018	NC		One	Background Prior	T	✓	0.698~0.830
23	SCDL [79]	2018	DSP	<i>NLR</i> (0.75K) + <i>NJU</i> (1.0K)	Two	Silhouette Feature, Spatial Coherence Loss	D		
24	PCF [48]	2018	CVPR	<i>NLR</i> (0.70K) + <i>NJU</i> (1.5K)	Three	Complementarity-Aware Fusion module [48]	D		0.827~0.925
25	CTMF [42]	2018	Cybernetic	<i>NLR</i> (0.70K) + <i>NJU</i> (1.5K)	Four	HHA [80], IPT, Hidden Structure Transfer	D		0.829~0.932
26	ACCF [81]	2018	IROS	<i>NLR</i> (0.70K) + <i>NJU</i> (1.5K)	Three	Attention-Aware	D		
27	PDNet [47]	2019	ICME	<i>NLR</i> (0.50K) + <i>NJU</i> (1.5K) + <i>O</i> (21K)		Depth-Enhanced Net [47]	D		
28	AFNet [61]	2019	arXiv	<i>NLR</i> (0.70K) + <i>NJU</i> (1.5K)	Three	Switch map, Edge-Aware loss	D		0.807~0.887
29	MMCI [82]	2019	PR	<i>NLR</i> (0.70K) + <i>NJU</i> (1.5K)	Three	HHA [80], Dilated Convolutional	D		0.839~0.928
30	TANet [83]	2019	TIP	<i>NLR</i> (0.70K) + <i>NJU</i> (1.5K)	Three	Attention-Aware Multi-Modal Fusion	D		0.847~0.941
31	CPFP [50]	2019	CVPR	<i>NLR</i> (0.70K) + <i>NJU</i> (1.5K)		Contrast Prior, Fluid Pyramid	D		0.852~0.932
32	D³Net (Ours)	2019		<i>NLR</i> (0.70K) + <i>NJU</i> (1.5K)	Seven	Depth Depurator Unit	D		0.864~0.946

depth-depurator unit to explicitly exclude low-quality depth maps when learning complementary feature by PDC [84] module.

III. PROPOSED DATASET

A. Dataset Overview

We introduce *SIP* dataset, the first human activities oriented salient person detection dataset. Our dataset contains 1K RGB-D images belonging to 8 different background scenes and 2 different lighting conditions, and performed by multiple actors. Each of them wear different cloths in different images. Following [70], the images are carefully selected to cover diverse challenging cases (*e.g.*, appearance change, occlusion, and shape complexity, *etc.*). Examples can be found in Fig. 2. The overall dataset can be downloaded from our website <http://dpfan.net/SIPDataset/>.

B. Sensors and Data Acquisition

Image Collection: We use the Huawei Mate 10 to collect our images. The Mate 10's rear cameras feature a high-grade Leica SUMMILUX-H lenses with bright f/1.6 apertures and combine 12MP RGB and 20MP Monochrome (Gray) sensors.

The depth map is automatically estimated by the Mate10. We asked nine people, all dressed in different colors, to perform the actions in real-world daily scenes. Instructions on how to perform the action to cover different challenging situations (*e.g.*, occlusion, out-of-view) were given, however, no instructions about style, angle, or speed were provided, so that record realistic data.

Data Annotation: After capturing 5,269 images and the corresponding depth maps, we first manually selected about 2,500 images, each of which includes one or multiple salient people. Following many famous SOD datasets [18], [57], [71], [72], [85]–[91], six viewers are further instructed to draw the bounding boxes (bboxes) according to their first glance at the most attention-grabbing person. We adopt the voting scheme described in [38] to discard those images with low voting consistency and choose top 1,000 satisfactory images. Second, another five annotators are introduced to label the accurate silhouettes of the salient objects according to the bboxes.

C. Dataset Statistics

Center Bias: In the field of visual saliency analysis, center bias has been identified as one of the most significant bias of saliency detection datasets [92]. It relates to the phenomenon

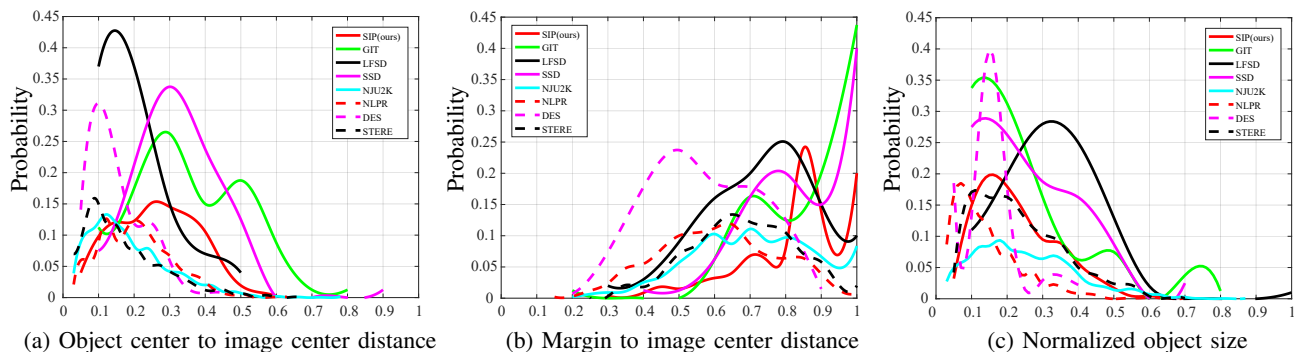


Fig. 3. (a) Distribution of normalized object center distance from image center. (b) Distribution of normalized object margin (farthest point in an object) distance from image center. (c) Distribution of normalized object size.

TABLE III
STATISTICS REGARDING CAMERA/OBJECT MOTIONS AND SALIENT OBJECT INSTANCE NUMBERS IN *SIP* DATASET.

<i>SIP</i> (Ours)	Background Objects								Lighting Conditions		# Object			
	car	flower	grass	road	tree	signs	barrier	other	low-light	sunny or cloudy	1	2	3	≥ 4
#Img	107	38	154	140	97	45	366	53	233	767	591	159	161	89

that subjects look more often at the center of the screen [93]. As noticed in [70], simply overlap all of the maps in the dataset can not describe the degree of center bias.

Following [70], we present the statistics of two distance R_o and R_m in Fig. 3 (a & b), where R_o and R_m indicate how far an object center and margin (farthest) point in an object are from the image center, respectively. The center bias of our *SIP* and existing [35]–[38], [63]–[65] datasets are shown in Fig. 3 (a & b). Except for our *SIP* and two small-scale datasets (*GIT* and *SSD*), most datasets present a high degree of center bias, *i.e.* the center of the object is close to the image center.

Size of Object: We define the object size as the ratio of salient object pixels to the image. As shown in Fig. 3 (c), the probability of normalized object size in *SIP* are 0.48%~66.85% (avg.: 20.43%).

Background Objects: As summarized in Table III, *SIP* includes diverse background objects (*e.g.*, car, tree, and grass, *etc.*). Models tested on such dataset could potentially handle realistic scenes better and thus are more practical.

Lighting Conditions: In Table III, we show different illumination conditions (*e.g.*, low-light, cloudy or sunny) in our *SIP* dataset. One example of the low-light condition can be found in Fig. 2, which often occurs in daily scenes. In addition, the depth map obtained in low-light condition inevitably brings up more challenges for detecting salient objects.

Amount of Salient Object: From Table I, we note that existing datasets fall in short of limited numbers (*e.g.*, ~one) of salient object. Previous studies [94], however, show that human could accurately enumerate up to at least 5 objects without counting. Thus, our *SIP* is collected containing less than 6 salient object per-image. The statistics of labelled objects in each image are shown in Table III (# Object).

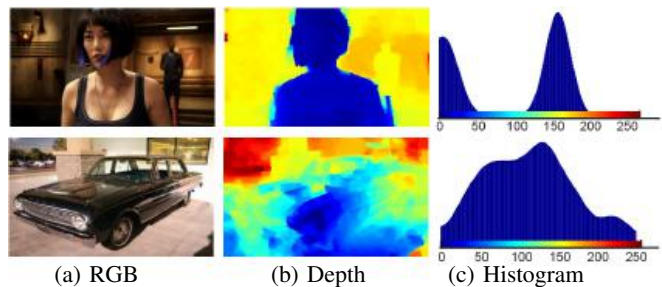


Fig. 4. The smoothed histogram (c) of high-quality (1st row), low-quality (2nd row) depth map, respectively.

IV. PROPOSED MODEL

The proposed simple baseline model D^3 Net contains two components, *e.g.*, a *depth depurator unit* (DDU) and a *feature learning module*. The DDU is utilized for explicitly filtering out the initial low-quality depth map. The latter one is used to extract the cross-modal feature sufficiently. These components form a nested structure (illustrated in Fig. 5), which are elaborately designed to achieve robust performance and high generalization ability on various challenging datasets.

A. Depth Depurator Unit (DDU)

Low-quality depth map adds more noise than signal to the prediction. The goal of DDU is to classify depth map into reasonable and low quality ones and not use the poor ones in the pipeline. As illustrated in Fig. 4 (b), a stand-alone salient object in high-quality depth map is typically characterized by well-defined closed boundaries and shows clear double peaks in its depth distribution. The statistics of the depth maps in existing datasets [36]–[38], [63]–[65] also support this phenomenon that is “*high quality depth maps usually contain clear objects, but the elements in low-quality depth maps are cluttered* (2nd row in Fig. 4)”.

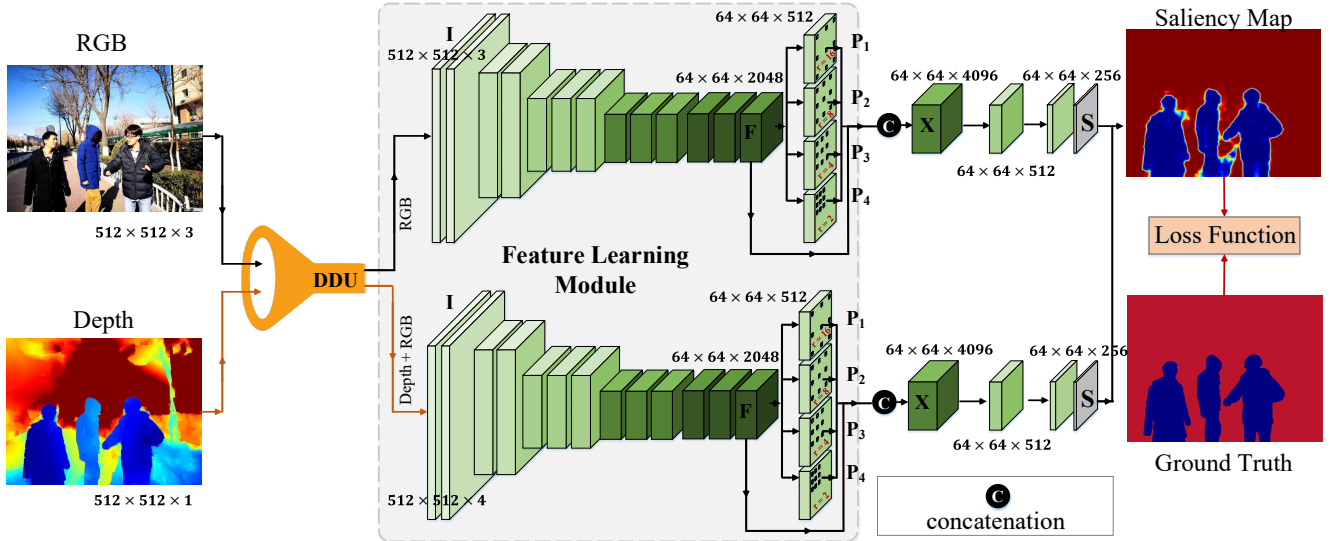


Fig. 5. Architecture overview of the proposed Deep Depth Depurator Network (D³Net), which consists of two components, *e.g.*, a depth depurator unit (DDU) (Section IV-A) and a feature learning module based on Pyramid Dilated Convolution (PDC) (Section IV-B).

In order to reject the low-quality depth maps, we propose DDU as the following: Firstly, the depth map has been re-sized to a fixed size (*e.g.*, 256×256) to reduce the computational complexity. To utilize these observation for efficiently filtering the low-quality depth maps, we then apply Otsu [95] algorithm to compute optimal threshold \mathbf{t}^* for each input depth S_d map:

$$\mathbf{t}^* = \arg \max_{\mathbf{t}} (\sigma_{S_d > \mathbf{t}}^2 - \sigma_{S_d \leq \mathbf{t}}^2), \quad (1)$$

where $\mathbf{t} \in \{0, 1, \dots, 255\}$, $\sigma_{S_d > \mathbf{t}}^2$ and $\sigma_{S_d \leq \mathbf{t}}^2$ is a variance of the salient region $S_d > \mathbf{t}$ and the non-salient region $S_d \leq \mathbf{t}$, respectively.

We use H to measure how much the object differs between the salient region and non-salient region. H will be high if the salient object of pixels is clearly distinguishable from its background. The H can be represented as,

$$H = |\mu(S_d \leq \mathbf{t}^*) - \mu(S_d > \mathbf{t}^*)|, \quad (2)$$

where μ is the mean value of the salient/non-salient region in depth map. Inspired by recent work using variance of non-salient region as characteristics for high-quality saliency map [58], we formulate the energy E of depth map by using the variance of the non-salient region:

$$E = \sigma^2(S_d > \mathbf{t}^*). \quad (3)$$

We further concat H and E feature as a simple combined feature is technically 1D co-feature $\mathbf{HE}_d = [H, E]$ for each depth map. To efficiently depurating the low-quality depth map, we follow the general idea of the regression tree [96] to classify the depth image.

$$\mathbf{x}_d = RTree(\mathbf{HE}_d, \mathbf{y}_d; \theta), \quad (4)$$

where $\mathbf{x}_d \in \{0, 1\}$, $\mathbf{y}_d \in \{0, 1\}$, and θ are predicted label (0 denotes low-quality map; 1 indicates normal map.), ground-truth label, and the parameter of regression tree, respectively.

B. Feature Learning Module

We design a feature learning module (FLM) that extracts features and learns the saliency map from RGB and optional Depth inputs. The FML is coupled with DDU such that when the output (\mathbf{x}_d) of the DDU module is equal to 1, we provide the RGB-D channel as the input of the feature learning module. Otherwise, we use the RGB channel.

Previous works in video SOD [7] and semantic segmentation [97] emphasized the efficiency of Pyramid Dilated Convolution (PDC). For simplicity, we use the standard ResNet-50 [98] cascaded with a PDC [84] module to extract spatial features, but our dilated rate is slight different from [84]. As shown in Fig. 5 (lower stream), let $\mathbf{F} \in \mathbb{R}^{W \times H \times M}$ denote a three-dimensional feature tensor of the input RGB-D image $\mathbf{I} \in \mathbb{R}^{W \times H \times 4}$. Then a set of parallel dilated convolution layers with kernels $\{\mathbf{D}_{r_k}\}_{k=1}^K$ and different dilation factors $\{r_k\}_{k=1}^K$ are adopted to \mathbf{F} to generate a set of cascaded feature maps $\{\mathbf{P}_k \in \mathbb{R}^{W \times H \times M}\}$:

$$\mathbf{P}_k = \mathbf{D}_{r_k} * \mathbf{F}, \quad (5)$$

where $*$ denotes the convolution operation. To address the degradation issue and learn the multi-scale features $\mathbf{Q} = \{\mathbf{P}_k\}_{k=1}^K$ automatically, we combine the input original feature \mathbf{F} and \mathbf{Q} as:

$$\mathbf{X} = [\mathbf{Q}, \mathbf{F}] = [\mathbf{P}_1, \mathbf{P}_2, \dots, \mathbf{P}_K, \mathbf{F}], \quad (6)$$

where $[\dots]$ denotes the concatenation operation and $\mathbf{X} \in \mathbb{R}^{W \times H \times (M + KM)}$. A 3×3 conv kernel with 512 channels (\mathbf{W}) and another 3×3 conv kernel with 256 channels (\mathbf{V}) are applied for feature dimension reduction progressively. To generate the final saliency map, we simply introduce another 1×1 conv kernel with 1 channel as a salient object readout function and use the sigmoid σ as activate function:

$$\mathbf{S} = \sigma(\mathbf{V} * (\mathbf{W} * \mathbf{X})), \quad (7)$$

Following [84], our PDC module has a similar structure with ASPP [97]. However, the ASPP treat different scales feature equally and apply element-wise sum operation (\oplus) on the output features: $\mathbf{X} = \mathbf{P}_1 \oplus \mathbf{P}_1 \oplus \dots \oplus \mathbf{P}_K$. Differently, our dilate

rate in the PDC is more larger in order to perceive more information from different scales.

C. Implementation Details

DDU. To learn the parameter of θ in the regression tree, we need to assign the quality label for each depth map in the training data. First, we compute the S-measure similarity score between the ground-truth map and the depth map. If the S-measure < 0.45 , we label this depth map as low-quality label (denote as 0). The rest depth maps are assigned middle or high quality label (denote as 1). Thus, the DDU is introduced to decide the quality of the depth is low or not. We randomly select about 1.4k image from NJU2K dataset as our training images and the level of regression tree is set to 5.

PDC Module. The alternative backbone network can be VGG-16 or ResNet-101, *etc.* The conv strides of the last two blocks are changed to 1. The input image is resized to 512×512 . The four dilation factors are set as $r_0 = 1, r_k = 12 * k$ ($k = \{1, 2, 3\}$). For the upper stream of PDC module, we use the RGB image to train this module. However, the lower stream of the PDC module is trained with the RGB and Depth image to learn cross-module features.

Loss Function. We adopt the widely-used cross entropy loss function L to train our model:

$$L(\mathbf{S}, \mathbf{G}) = -\frac{1}{N} \sum_{i=1}^N (g_i \log(s_i) + (1 - g_i) \log(1 - s_i)), \quad (8)$$

where $\mathbf{S} \in \{0, 1\}^{512 \times 512}$ and $\mathbf{G} \in \{0, 1\}^{512 \times 512}$ indicates the estimated saliency map and the GT map, respectively. $g_i \in \mathbf{G}$, $s_i \in \mathbf{S}$, and N denotes the total number of pixels.

Training Settings. For fair comparisons, we follow the same training settings described in [50]. We randomly sample 1400 image pairs and 650 image pairs from the *NJU2K* [36] and *NLPR* [38] datasets as the training set, 100 and 50 image pairs from the *NJU2K* and *NLPR* datasets as the validation set for hyper-parameter tuning (*e.g.*, base learning rate). The proposed D³Net is implemented using Python, with the Pytorch toolbox. We adopt the SGD [99] as the optimizer and the initial learning rate is 0.007. The iteration number is set as 165000. The momentum and weight decay are set to 0.9, and $5e-4$, respectively.

Data Augmentation. Due to the limited scale of existing datasets, we augment the training samples by mirror reflection, rotation (from $0^\circ \sim 180^\circ$ randomly), and image cropping (following [82]) to overcome the risk of overfitting. The total training time is about 50 hours on GTX TITAN X GPU with 12G memory.

V. BENCHMARKING EVALUATION RESULTS

We benchmark about 91K (5,398 images \times 17 models) images in this study, making it the largest and most comprehensive RGB-D based SOD benchmark to date.

A. Experimental Settings

Models. We benchmark 17 SOTA models (see Table V) including 10 traditional and 7 CNNs based models.

Datasets. We conduct our experiments on seven datasets (see Table V). The test sets of *NJU2K* [36] and *NLPR* [38]

datasets, and the whole *STERE* [63], *DES* [37], *SSD* [64], *LFSD* [65], and *SIP* datasets are used for testing.

Runtime. In Table IV we summarize the runtime of existing approaches. The timings are tested on the same platform: Intel Xeon(R) E5-2676v3 2.4GHz \times 24 and GTX TITAN X. Since [42], [46], [48], [66]–[68], [81]–[83] did not release codes, the timings are borrowed from original paper or provided by authors. Our D³Net does not apply post-processing (*e.g.*, CRF), thus the computation only takes about 0.05s (DDU 0.01 + PDC 0.04) for a 224×224 image.

B. Evaluation Metrics

MAE M . We follow Perazzi *et al.* [100] to evaluate the *mean absolute error* (MAE) between a real-valued saliency map Sal and a binary ground-truth G for all image pixels:

$$MAE = \frac{1}{N} |Sal - G|, \quad (9)$$

where N is the total number of pixels. The MAE estimates the approximation degree between the saliency map and the ground-truth map, and it is normalized to $[0, 1]$. The MAE provides a direct estimate of conformity between estimated and ground-truth maps. However, for the MAE metric, small objects naturally assign a smaller error and larger objects have larger errors. The metric also can not tell where the error occurs [101].

PR Curve. We also follow Borji *et al.* [5] to provide the PR Curve. We divide the saliency map S using a fixed threshold which changes from 0 to 255. For each threshold, a pair of recall&precision scores are computed, and are finally combined to form a precision-recall curve to describe the model performance at different situations. The overall evaluation results of PR Curve are shown in Fig. 6 and Fig. 8.

F-measure F_β . F-measure is essentially a region based similarity metric. Following Cheng and Zhang *et al.* works [5], [102], we also provide the max F-measure using varying fixed (0-255) thresholds. The overall evaluation results of F-measure under different thresholds on each dataset are shown in Fig. 7 and Fig. 8.

S-measure S_α . Both MAE and F-measure metrics ignore the important structure information evaluation, whereas behavioral vision studies have shown that the human visual system is highly sensitive to structures in scenes [58]. Thus, we additionally include the structure measure (S-measure [58]). The S-measure combines the region-aware (S_r) and object-aware (S_o) structural similarity as their final structure metric:

$$S_\alpha = \alpha * S_o + (1 - \alpha) * S_r, \quad (10)$$

where $\alpha \in [0, 1]$ is the balance parameter and set to 0.5 as default.

E-measure E_ξ . E-measure is the recent proposed Enhanced alignment measure [59] in the binary map evaluation field. This measure based on cognitive vision studies, which combines local pixel values with the image-level mean value in one term, jointly capturing image-level statistics and local pixel matching information. Here, we introduce it to provide a more comprehensive evaluation.

TABLE IV
THE RUNTIME OF EXISTING APPROACHES. “*” INDICATES CPU TIME AND THE OTHERS INDICATE GPU TIME. ‡ DONATES THE DEEP-LEARNING BASED MODEL. M = MATLAB. PY = PYTHON. TF = TENSORFLOW. N.A. = NOT AVAILABLE.

Method	LHM [38]	DESM [37]	ACSD [36]	GP [39]	LBE [40]	DCMC [55]	SE [41]	CDPC [45]
Time (s)	2.130*	7.790*	0.718*	12.98*	3.110*	1.200*	1.570*	>60.0*
Code Type	M	M	C++	M&C++	M&C++	M	M&C++	M&C++
Method	DF‡ [43]	MDSF [44]	MCLP [66]	HSCS [67]	ICS [68]	CDB [46]	PCF‡ [48]	CTMF‡ [42]
Time (s)	10.36	>60.0*	41.03*	8.290*	42.67*	0.600*	0.060	0.630
Code Type	M&C++	C++	N.A.	N.A.	N.A.	M	Caffe	Caffe
Method	ACCF‡ [81]	PDNet‡ [47]	AFNet‡ [61]	MMCI‡ [82]	TANet‡ [83]	CPFP‡ [50]	D³Net (Ours)‡	
Time (s)	0.060	0.067	0.030	0.050	0.070	0.170	0.050	
Code Type	Caffe	Py&Caffe	Tf	Caffe	Caffe	Caffe	Pytorch	

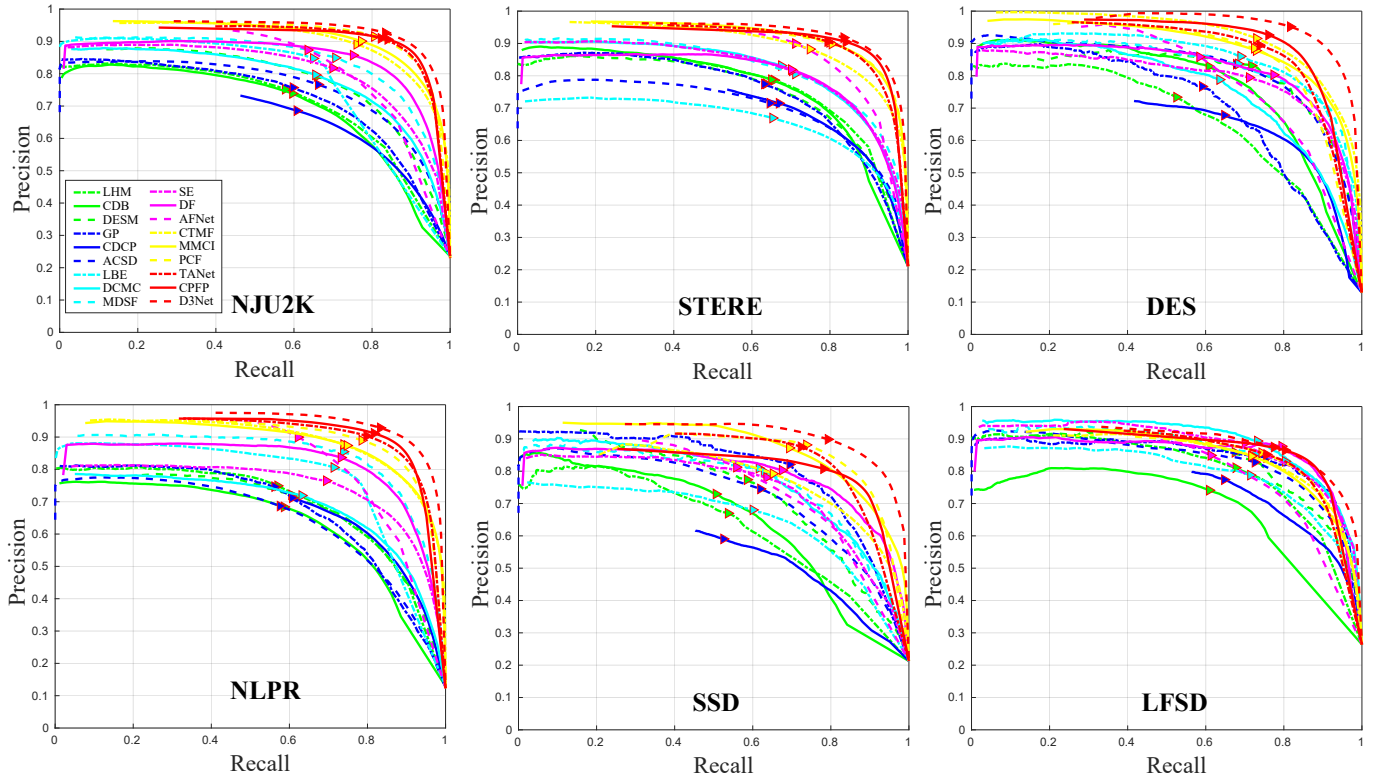


Fig. 6. PR Curve on six datasets, using varying fixed threshold.

C. Metric Statistics

For a given metric $\zeta \in \{S_\alpha, F_\beta, E_\xi, M\}$ we consider different statistics. I_j^i denote the image of specific dataset D_i . Thus, $D_i = \{I_1^i, I_2^i, \dots, I_j^i\}$. Let $\bar{\zeta}(I_j^i)$ be the metric score on image I_j^i . The mean is the average dataset statistic defined as $M_\zeta(D_i) = \frac{1}{|D_i|} \sum \bar{\zeta}(I_j^i)$. Where $|D_i|$ is the total number of images on the D_i dataset. The mean statistic over different datasets are summarized in Table V.

D. Performance Comparison and Analysis

Performance of Traditional Models. Based on the overall performance listed in Table V, we observe that “SE [41], MDSF [44], and DCMC [55] are top 3 traditional algorithms.” Utilizing superpixel technology, both SE and DCMC explicitly extract the region contrast features from RGB image.

In contrast, MDSF formulate SOD as a pixel-wise binary labeling problem, which is solved by SVM.

Performance of Deep Models. our D³Net, CPFP [50] and TANet [83] are top 3 deep models compared to other leading methods, showing the strong feature representation ability of deep learning for this task.

Traditional vs Deep Models. From Table V, we observe that most of the deep models perform better than the traditional algorithms. Interestingly, the MDSF [64] outperforms two deep models (*i.e.*, DF [43] and AFNet [61]) on NLPR dataset.

E. Comparison with SOTAs

We compared our D³Net vs. 17 SOTA models in Table V. In general, our model outperforms the best published result (CPFP [50]-CVPR’19) by a large margin of 1.2% ~ 5.9% on

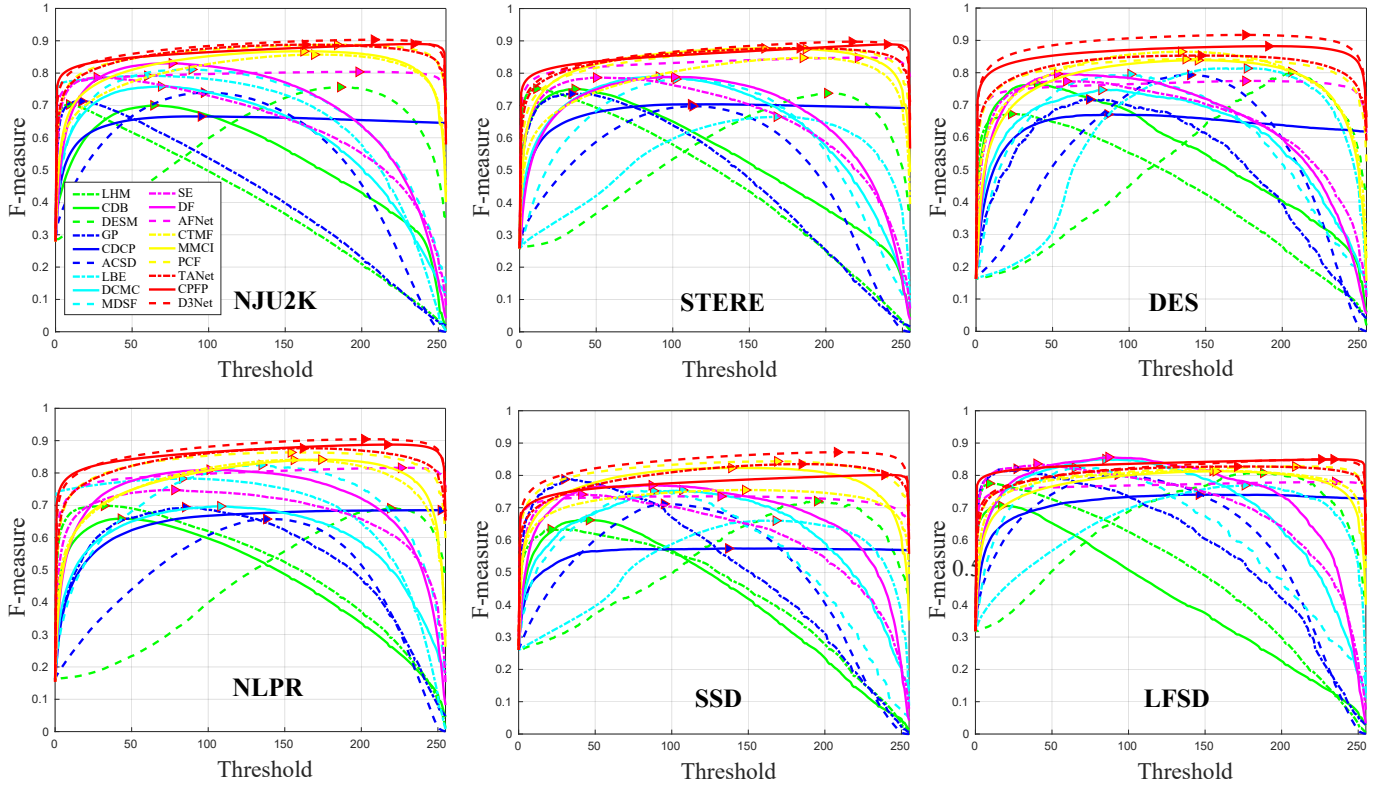


Fig. 7. F-measures under different thresholds on six datasets.

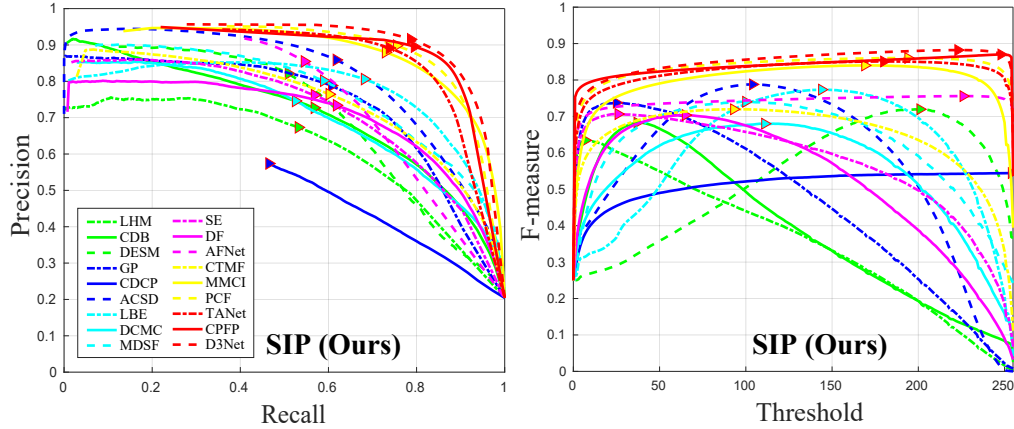


Fig. 8. PR Curve and F-measures under different thresholds on the proposed SIP datasets.

6 datasets. Notably, we still achieve significant improvements of 1.4% on the proposed real-world *SIP* dataset.

We also report saliency maps generated on various challenging scenes to show the superiority of our D^3 Net visually. Some representative examples are shown in Fig. 9 such as the structure of the salient object in depth map are partially (*e.g.*, the 1st, 4th, and 5th rows) or dramatically (*i.e.*, the 2nd-3rd rows) damaged. Especially, in the 3rd and 5th rows, the depth of the salient object is locally connected with background scenes. Also, the 4th row contains multiple isolated salient objects. For these challenging situations, most of existing top

competitors are unlikely to locate the salient objects due to the poor depth maps or insufficient multi-modal fusion schemes. Although the CPF [50], TANet [83], and PCF [48] can generate more correct saliency maps than others, the salient object often introduce noticeable distinguished backgrounds (3rd-5th rows) or lost fine details of salient object (1st row) due to the deficiency of cross-modality learning ability. In contrast, our baseline model is able to eliminate low-quality depth maps and adaptively select complementary information from RGB and Depth image to infer the real salient object and highlight its details.

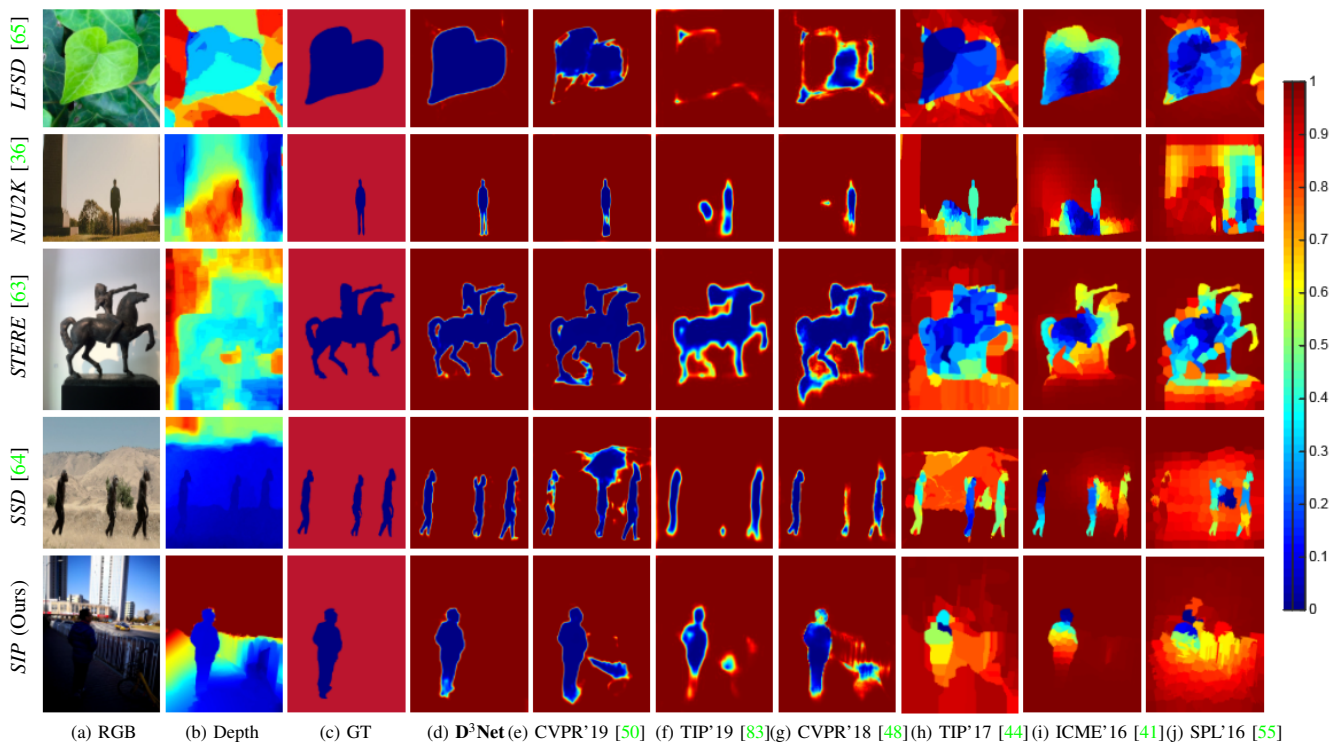


Fig. 9. Visual comparisons with top 3 CNNs-based (CPFP [50], TANet [83], and PCF [48]) models and 3 classical non-deep (MDSF [44], SE [44] and DCMC [55]) methods on five datasets. Further results in the <http://dpfan.net/D3NetBenchmark>.

VI. BACKGROUND CHANGED BOOK COVER APPLICATION

Background change techniques become vital for designers to leverage the increasing volumes of available image database. Traditional designers utilize the photoshop tool to design their products. This is a quite time-consuming task and requires much basic technical knowledge.

A large majority of potential users fail to grasp the technique in the design. Thus an easy-to-use application is needed. Previous similar work, such as automatic generation of visual-textual application [103], [104] motivate us to create the background change application.

To overcome such drawbacks, the salient object detection technology would be a potential solution strategy. We define a background change application prototype demo, as shown in Fig. 10. First, the user can upload one image which is a candidate designed image. Then, content-based image features such as a RGB-D based saliency map should also be considered in the automatic generation of salient object. Finally, the system allows us to choose from our library of professionally designed book cover layouts. By combining high-level template constraints and low-level image features, we obtain the background changed book cover as shown in Fig. 10 (c).

Since this is not our main focus in this article, we following yang *et al.* [103] to set our visual background image with a specified topic [104]. In the stage two, the input image should be resized (the first row example of Fig. 10) to matched to the target style size and preserve the salient region according to our inference of our D³Net model.



(a) Input Image (b) Salient Object (c) Background Changed

Fig. 10. Examples of book cover maker. See Section VI for details.

VII. DISCUSSION

Based on our comprehensive benchmarking results, we present our conclusion to the most important questions that may benefit the research community to rethink the RGB-D image for salient object detection.

Ablation study. Now we provide detailed analysis of the proposed baseline model D³Net. To verify the effectiveness of the depth map filter mechanism, we derive two baselines: Base1 and Base2, refer to our PDC module using the RGB (upper stream in Fig. 5) or RGB-D image (lower stream).

TABLE VI
PERFORMANCE OF S-MEASURE \uparrow ON OUR *SIP* AND *STERE* DATASET. THESE DIFFERENCES ARE ALL STATISTICALLY SIGNIFICANT AT THE $\alpha < 0.05$ LEVEL. THE \uparrow INDICATES THAT THE HIGHER THE SCORE IS, THE BETTER THE MODEL PERFORMS AND VICE VERSA. SEE DETAILS IN SECTION VII.

Aspects	Model	<i>SIP (Ours)</i>	<i>STERE</i> [63]
Deep-based	PCF [48]	0.842	0.875
	TANet [43]	0.835	0.871
	CPFP [42]	0.850	0.879
w/o DDU	Base1 (RGB channel)	0.843	0.880
	Base2 (RGB-D channel)	0.850	0.878
DDU	D³Net (Ours)	0.864	0.891

In Table VI, we observe that Base2 performs better than Base1 on the *SIP* dataset. More specially, the improvement is 0.7% (0.850%-0.843%). However, the Base2 decreases the S-measure score on the *STERE* dataset compared to the Base1. Because the *STERE* contains a large amount (92%) of low-quality of depth maps. These results suggest that initial low-quality depth map may introduce misleading saliency cues.

Is the DDU helpful? Yes. To further validate the effectiveness of our DDU module, we provide another baseline: Base1 & Base2, which consists of only PDC module. From Table VI, we find that the use of DDU improves performance to a certain extent. We attribute the improvement to the DDU that can discard low-quality depth map and select one optimal path (Base1 or Base2). It is worth mentioning that D³Net outperforms any prior approach intended for SOD without any post-processing techniques such as CRF that are typically used to boost scores.

A. Limitations

First, it is worth pointing out that the number of the images in the *SIP* dataset is relatively smaller compared with most datasets for RGB images saliency detection. Our goal of built this dataset is to explore the potential direction of smart phone based application. As can be seen from the benchmark results and the demo application described in Section VI, the salient object detection over real human activities scenes is a promising direction. We plan to keep growing the dataset with more challenging situations and various kinds of foreground person. Second, our simple baseline D³Net consists of two networks which may increase the memory on the lightweight device. In real environment, some possible strategies can also be considered in this baseline model such as replace the ResNet-50 backbone with MobileNet V2 [105] or the recent released ESPNet V2 [106] models.

VIII. CONCLUSION

We present systematic studies on RGB-D based salient object detection by (1) introducing a new human-oriented *SIP* dataset reflecting the realistic in-the-wild mobile use scenarios. (2) designing a novel D³Net model. (3) conducting so far the largest-scale (~91K) benchmark. Compared with existing datasets, *SIP* conforms to several characteristics of human in the real environments (*e.g.*, background diversity, occlusion,

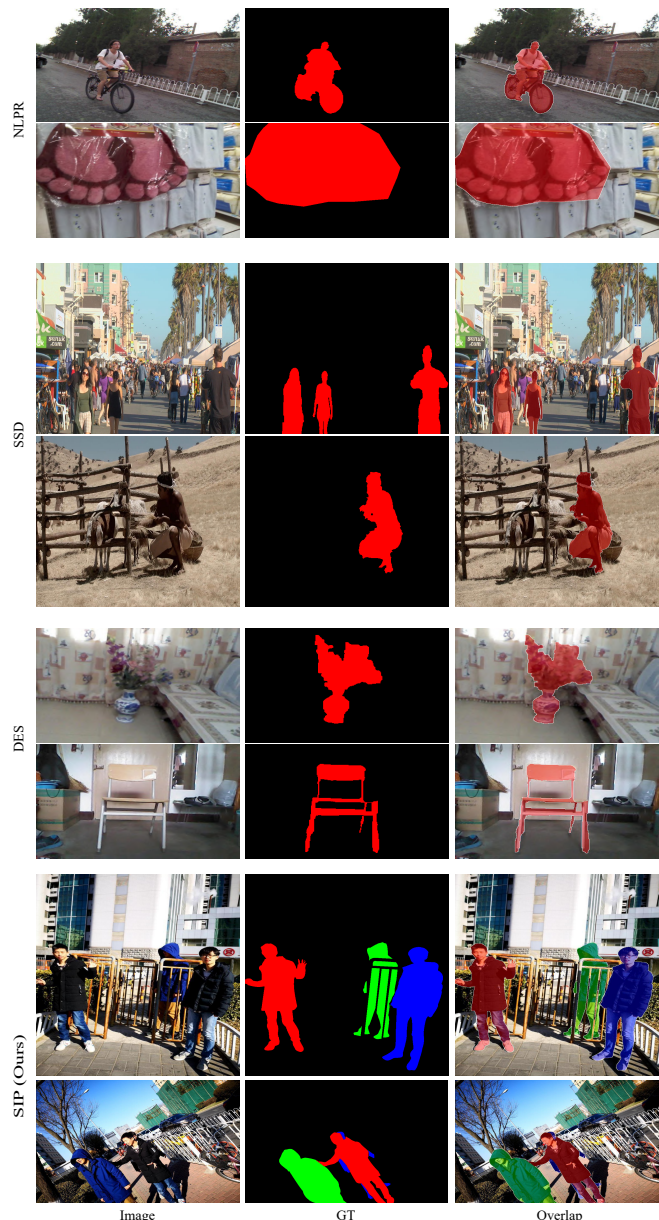


Fig. 11. Compared with previous object-level datasets which are labeled with coarse boundary (the spoke in *NLRP* [38], the flower in *DES* [37], the person in *SSD* [64]) or polygons (*e.g.*, foot pad in *NLRP*). However, the proposed object-instance-level *SIP* dataset is labeled with smooth fine boundaries. More specifically, the occlusion situation is also considered (*e.g.*, the barrier region).

etc.) Moreover, the proposed baseline achieves promising results. It is among the fastest methods, making it a practical solution. The comprehensive benchmarking results include 31 summarized SOTA methods and 17 evaluated traditional/deep models. We hope this benchmark would not only accelerate the development of this area but also others (*e.g.*, stereo estimating/matching [107], multiple salient person detection, and salient instance detection [18]). We foresee this study would drive the salient object detection toward real-world application scenario with multiple salient persons and complex interactions through the mobile device (*e.g.*, smart phone or tablet).

REFERENCES

- [1] W. Wang, Q. Lai, H. Fu, J. Shen, and H. Ling, "Salient object detection in the deep learning era: An in-depth survey," *arXiv preprint arXiv:1904.09146*, 2019.
- [2] T. Wang, L. Zhang, S. Wang, H. Lu, G. Yang, X. Ruan, and A. Borji, "Detect globally, refine locally: A novel approach to saliency detection," in *IEEE CVPR*, 2018, pp. 3127–3135.
- [3] H. Fu, D. Xu, S. Lin, and J. Liu, "Object-based rgbd image co-segmentation with mutex constraint," in *CVPR*, 2015, pp. 4428–4436.
- [4] P. Zhang, W. Liu, H. Lu, and C. Shen, "Salient object detection with lossless feature reflection and weighted structural loss," *IEEE TIP*, 2019.
- [5] A. Borji, M.-M. Cheng, H. Jiang, and J. Li, "Salient Object Detection: A Benchmark," *IEEE TIP*, vol. 24, no. 12, pp. 5706–5722, 2015.
- [6] W. Wang, J. Shen, J. Xie, M.-M. Cheng, H. Ling, and A. Borji, "Revisiting video saliency prediction in the deep learning era," *TPAMI*, 2019.
- [7] D.-P. Fan, W. Wang, M.-M. Cheng, and J. Shen, "Shifting more attention to video salient object detection," in *IEEE CVPR*, 2019.
- [8] Y. Zeng, Y. Zhuge, H. Lu, and L. Zhang, "Multi-source weak supervision for saliency detection," in *IEEE CVPR*, 2019.
- [9] R. Wu, M. Feng, W. Guan, and D. Wang, "A mutual learning method for salient object detection with intertwined multi-supervision," in *IEEE CVPR*, 2019.
- [10] L. Zhang, i. Zhang, Z. Lin, H. Lu, and Y. He, "Capsal: Leveraging captioning to boost semantics for salient object detection," in *IEEE CVPR*, 2019.
- [11] M. Feng, H. Lu, and E. Ding, "Attentive feedback network for boundary-aware salient object detection," in *IEEE CVPR*, 2019.
- [12] X. Hu, L. Zhu, J. Qin, C.-W. Fu, and P.-A. Heng, "Recurrently aggregating deep features for salient object detection," in *AAAI*, 2018.
- [13] L. Wang, L. Wang, H. Lu, P. Zhang, and X. Ruan, "Salient object detection with recurrent fully convolutional networks," *IEEE TPAMI*, 2018.
- [14] Y. Xu, X. Hong, F. Porikli, X. Liu, J. Chen, and G. Zhao, "Saliency integration: An arbitrator model," *IEEE TMM*, vol. 21, no. 1, pp. 98–113, 2019.
- [15] N. Liu, J. Han, and M.-H. Yang, "PiCANet: Learning Pixel-wise Contextual Attention for Saliency Detection," in *IEEE CVPR*, 2018, pp. 3089–3098.
- [16] Z. Deng, X. Hu, L. Zhu, X. Xu, J. Qin, G. Han, and P.-A. Heng, "R3Net: recurrent residual refinement network for saliency detection," in *IJCAI*, 2018, pp. 684–690.
- [17] Q. Hou, M.-M. Cheng, X. Hu, A. Borji, Z. Tu, and P. Torr, "Deeply supervised salient object detection with short connections," *IEEE TPAMI*, vol. 41, no. 4, pp. 815–828, 2019.
- [18] G. Li, Y. Xie, L. Lin, and Y. Yu, "Instance-level salient object segmentation," in *IEEE CVPR*, 2017, pp. 247–256.
- [19] M. A. Islam, M. Kalash, M. Rochan, N. Bruce, and Y. Wang, "Salient object detection using a context-aware refinement network," in *BMVC*, 2017.
- [20] Z. Luo, A. Mishra, A. Achkar, J. Eichel, S. Li, and P.-M. Jodoin, "Non-local deep features for salient object detection," in *IEEE CVPR*, 2017, pp. 6609–6617.
- [21] T. Chen, L. Lin, L. Liu, X. Luo, and X. Li, "DISC: Deep Image Saliency Computing via Progressive Representation Learning," *IEEE TNNLS*, vol. 27, no. 6, pp. 1135–1149, 2016.
- [22] G. Lee, Y.-W. Tai, and J. Kim, "Deep saliency with encoded low level distance map and high level features," in *IEEE CVPR*, 2016, pp. 660–668.
- [23] R. Zhao, W. Ouyang, H. Li, and X. Wang, "Saliency detection by multi-context deep learning," in *IEEE CVPR*, 2015, pp. 1265–1274.
- [24] S. Chen, X. Tan, B. Wang, and X. Hu, "Reverse attention for salient object detection," in *ECCV*. Springer, 2018, pp. 234–250.
- [25] Y. Zhuge, Y. Zeng, and H. Lu, "Deep embedding features for salient object detection," in *AAAI*, 2019.
- [26] J. Su, J. Li, C. Xia, and Y. Tian, "Selectivity or invariance: Boundary-aware salient object detection," *arXiv preprint arXiv:1812.10066*, 2018.
- [27] P. Jiang, Z. Pan, N. Vasconcelos, B. Cheng, and J. Peng, "Super diffusion for salient object detection," *arXiv preprint arXiv:1811.09038*, 2018.
- [28] Z. Li, C. Lang, Y. Chen, J. Liew, and J. Feng, "Deep reasoning with multi-scale context for salient object detection," *arXiv preprint arXiv:1901.08362*, 2019.
- [29] S. Jia and N. D. Bruce, "Richer and deeper supervision network for salient object detection," *arXiv preprint arXiv:1901.02425*, 2019.
- [30] X. Huang and Y.-J. Zhang, "300-fps salient object detection via minimum directional contrast," *IEEE TIP*, vol. 26, no. 9, pp. 4243–4254, 2017.
- [31] X. Li, F. Yang, H. Cheng, W. Liu, and D. Shen, "Contour knowledge transfer for salient object detection," in *ECCV*. Springer, 2018, pp. 355–370.
- [32] M. Kummerer, T. S. A. Wallis, and M. Bethge, "Saliency benchmarking made easy: Separating models, maps and metrics," in *ECCV*. Springer, 2018.
- [33] X. Chen, A. Zheng, J. Li, and F. Lu, "Look, perceive and segment: Finding the salient objects in images via two-stream fixation-semantic cnns," in *IEEE ICCV*, 2017.
- [34] M. Amirul Islam, M. Kalash, and N. D. Bruce, "Revisiting salient object detection: Simultaneous detection, ranking, and subitizing of multiple salient objects," in *IEEE CVPR*, 2018, pp. 7142–7150.
- [35] A. Ciptadi, T. Hermans, and J. M. Rehg, "An in depth view of saliency," in *BMVC*, 2013.
- [36] R. Ju, L. Ge, W. Geng, T. Ren, and G. Wu, "Depth saliency based on anisotropic center-surround difference," in *IEEE ICIP*, 2014, pp. 1115–1119.
- [37] Y. Cheng, H. Fu, X. Wei, J. Xiao, and X. Cao, "Depth enhanced saliency detection method," in *ACM ICIMCS*, 2014, p. 23.
- [38] H. Peng, B. Li, W. Xiong, W. Hu, and R. Ji, "Rgbd salient object detection: a benchmark and algorithms," in *ECCV*. Springer, 2014, pp. 92–109.
- [39] J. Ren, X. Gong, L. Yu, W. Zhou, and M. Ying Yang, "Exploiting Global Priors for RGB-D Saliency Detection," in *IEEE CVPRW*, 2015, pp. 25–32.
- [40] D. Feng, N. Barnes, S. You, and C. McCarthy, "Local background enclosure for RGB-D salient object detection," in *IEEE CVPR*, 2016, pp. 2343–2350.
- [41] J. Guo, T. Ren, and J. Bei, "Salient object detection for rgb-d image via saliency evolution," in *IEEE ICME*, 2016, pp. 1–6.
- [42] J. Han, H. Chen, N. Liu, C. Yan, and X. Li, "CNNs-based RGB-D saliency detection via cross-view transfer and multiview fusion," *IEEE TOC*, 2018.
- [43] L. Qu, S. He, J. Zhang, J. Tian, Y. Tang, and Q. Yang, "RGBD salient object detection via deep fusion," *IEEE TIP*, vol. 26, no. 5, pp. 2274–2285, 2017.
- [44] H. Song, Z. Liu, H. Du, G. Sun, O. Le Meur, and T. Ren, "Depth-aware salient object detection and segmentation via multiscale discriminative saliency fusion and bootstrap learning," *IEEE TIP*, vol. 26, no. 9, pp. 4204–4216, 2017.
- [45] C. Zhu, G. Li, W. Wang, and R. Wang, "An innovative salient object detection using center-dark channel prior," in *IEEE ICCVW*, 2017.
- [46] F. Liang, L. Duan, W. Ma, Y. Qiao, Z. Cai, and L. Qing, "Stereoscopic saliency model using contrast and depth-guided-background prior," *Neurocomputing*, vol. 275, pp. 2227–2238, 2018.
- [47] C. Zhu, X. Cai, K. Huang, T. H. Li, and G. Li, "Pdnet: Prior-model guided depth-enhanced network for salient object detection," in *IEEE ICME*, 2019.
- [48] H. Chen and Y. Li, "Progressively Complementarity-Aware Fusion Network for RGB-D Salient Object Detection," in *IEEE CVPR*, 2018, pp. 3051–3060.
- [49] W. Wang, J. Shen, Y. Yu, and K.-L. Ma, "Stereoscopic thumbnail creation via efficient stereo saliency detection," *IEEE TVCG*, vol. 23, no. 8, pp. 2014–2027, 2017.
- [50] J.-X. Zhao, Y. Cao, D.-P. Fan, M.-M. Cheng, X.-Y. Li, and L. Zhang, "Contrast prior and fluid pyramid integration for rgbd salient object detection," in *IEEE CVPR*, 2019.
- [51] J. Zhao, J. Li, Y. Cheng, T. Sim, S. Yan, and J. Feng, "Understanding humans in crowded scenes: Deep nested adversarial learning and a new benchmark for multi-human parsing," in *ACM MM*, 2018, pp. 792–800.
- [52] Z. Zhang, "Microsoft kinect sensor and its effect," *IEEE TMM*, vol. 19, no. 2, pp. 4–10, 2012.
- [53] R. Ng, M. Levoy, M. Brédif, G. Duval, M. Horowitz, P. Hanrahan *et al.*, "Light field photography with a hand-held plenoptic camera," *Computer Science Technical Report (CSTR)*, vol. 2, no. 11, pp. 1–11, 2005.
- [54] C. Liu, J. Yuen, and A. Torralba, "Sift flow: Dense correspondence across scenes and its applications," *IEEE TPAMI*, vol. 33, no. 5, pp. 978–994, 2011.
- [55] R. Cong, J. Lei, C. Zhang, Q. Huang, X. Cao, and C. Hou, "Saliency detection for stereoscopic images based on depth confidence analysis and multiple cues fusion," *IEEE SPL*, vol. 23, no. 6, pp. 819–823, 2016.

- [56] R. Cong, J. Lei, H. Fu, M.-M. Cheng, W. Lin, and Q. Huang, "Review of visual saliency detection with comprehensive information," *IEEE TCSVT*, 2018.
- [57] R. Achanta, S. Hemami, F. Estrada, and S. Susstrunk, "Frequency-tuned salient region detection," in *IEEE CVPR*, 2009, pp. 1597–1604.
- [58] D.-P. Fan, M.-M. Cheng, Y. Liu, T. Li, and A. Borji, "Structure-measure: A new way to evaluate foreground maps," in *IEEE ICCV*, 2017, pp. 4548–4557.
- [59] D.-P. Fan, C. Gong, Y. Cao, B. Ren, M.-M. Cheng, and A. Borji, "Enhanced-alignment Measure for Binary Foreground Map Evaluation," in *IJCAI*, 2018, pp. 698–704.
- [60] R. Margolin, L. Zelnik-Manor, and A. Tal, "How to evaluate foreground maps?" in *IEEE CVPR*, 2014, pp. 248–255.
- [61] N. Wang and X. Gong, "Adaptive fusion for RGB-D salient object detection," *arXiv preprint arXiv:1901.01369*, 2019.
- [62] H. Du, Z. Liu, H. Song, L. Mei, and Z. Xu, "Improving rgbd saliency detection using progressive region classification and saliency fusion," *IEEE Access*, vol. 4, pp. 8987–8994, 2016.
- [63] Y. Niu, Y. Geng, X. Li, and F. Liu, "Leveraging stereopsis for saliency analysis," in *IEEE CVPR*, 2012, pp. 454–461.
- [64] C. Zhu and G. Li, "A Three-pathway Psychobiological Framework of Salient Object Detection Using Stereoscopic Technology," in *IEEE ICCVW*, 2017, pp. 3008–3014.
- [65] N. Li, J. Ye, Y. Ji, H. Ling, and J. Yu, "Saliency detection on light field," in *IEEE CVPR*, 2014, pp. 2806–2813.
- [66] R. Cong, J. Lei, H. Fu, W. Lin, Q. Huang, X. Cao, and C. Hou, "An iterative co-saliency framework for rgbd images," *IEEE TOC*, no. 99, pp. 1–14, 2017.
- [67] R. Cong, J. Lei, H. Fu, Q. Huang, X. Cao, and N. Ling, "Hscs: Hierarchical sparsity based co-saliency detection for rgbd images," *IEEE TMM*, 2018.
- [68] R. Cong, J. Lei, H. Fu, Q. Huang, X. Cao, and C. Hou, "Co-saliency detection for RGBD images based on multi-constraint feature matching and cross label propagation," *IEEE TIP*, vol. 27, no. 2, pp. 568–579, 2018.
- [69] D. Sun, S. Roth, and M. J. Black, "Secrets of optical flow estimation and their principles," in *IEEE CVPR*, 2010, pp. 2432–2439.
- [70] D.-P. Fan, J.-J. Liu, S.-H. Gao, Q. Hou, A. Borji, and M.-M. Cheng, "Salient objects in clutter: Bringing salient object detection to the foreground," in *ECCV*. Springer, 2018, pp. 1597–1604.
- [71] M.-M. Cheng, N. J. Mitra, X. Huang, P. H. S. Torr, and S.-M. Hu, "Global contrast based salient region detection," *IEEE TPAMI*, vol. 37, no. 3, pp. 569–582, 2015.
- [72] L. Wang, H. Lu, Y. Wang, M. Feng, D. Wang, B. Yin, and X. Ruan, "Learning to detect salient objects with image-level supervision," in *IEEE CVPR*, 2017, pp. 136–145.
- [73] P. Sauer, T. F. Cootes, and C. J. Taylor, "Accurate regression procedures for active appearance models," in *BMVC*, 2011, pp. 1–11.
- [74] K. Desingh, K. M. Krishna, D. Rajan, and C. Jawahar, "Depth really matters: Improving visual salient region detection with depth," in *BMVC*, 2013.
- [75] C.-C. Chang and C.-J. Lin, "LIBSVM: a library for support vector machines," *ACM TIST*, vol. 2, no. 3, p. 27, 2011.
- [76] X. Fan, Z. Liu, and G. Sun, "Salient region detection for stereoscopic images," in *IEEE DSP*, 2014, pp. 454–458.
- [77] R. Shigematsu, D. Feng, S. You, and N. Barnes, "Learning RGB-D salient object detection using background enclosure, depth contrast, and top-down features," in *IEEE ICCVW*, 2017, pp. 2749–2757.
- [78] A. Wang and M. Wang, "RGB-D salient object detection via minimum barrier distance transform and saliency fusion," *IEEE SPL*, vol. 24, no. 5, pp. 663–667, 2017.
- [79] P. Huang, C.-H. Shen, and H.-F. Hsiao, "Rgbd salient object detection using spatially coherent deep learning framework," in *IEEE DSP*, 2018, pp. 1–5.
- [80] S. Gupta, R. Girshick, P. Arbeláez, and J. Malik, "Learning rich features from RGB-D images for object detection and segmentation," in *ECCV*. Springer, 2014, pp. 345–360.
- [81] H. Chen, Y.-F. Li, and D. Su, "Attention-aware cross-modal cross-level fusion network for RGB-D salient object detection," in *IEEE IROS*, 2018, pp. 6821–6826.
- [82] H. Chen, Y. Li, and D. Su, "Multi-modal fusion network with multi-scale multi-path and cross-modal interactions for RGB-D salient object detection," *Pattern Recognition*, vol. 86, pp. 376–385, 2019.
- [83] H. Chen and Y. Li, "Three-stream attention-aware network for RGB-D salient object detection," *IEEE TIP*, 2019.
- [84] H. Song, W. Wang, S. Zhao, J. Sheng, and K.-M. Lam, "Pyramid dilated deeper convLSTM for video salient object detection," in *ECCV*, 2018.
- [85] S. Alpert, M. Galun, R. Basri, and A. Brandt, "Image segmentation by probabilistic bottom-up aggregation and cue integration," in *IEEE CVPR*, 2007, pp. 1–8.
- [86] H. Jiang, M.-M. Cheng, S.-J. Li, A. Borji, and J. Wang, "Joint Salient Object Detection and Existence Prediction," *Front. Comput. Sci.*, 2017.
- [87] G. Li and Y. Yu, "Visual saliency based on multiscale deep features," in *IEEE CVPR*, 2015, pp. 5455–5463.
- [88] T. Liu, J. Sun, N. Zheng, X. Tang, and H.-Y. Shum, "Learning to detect a salient object," in *IEEE CVPR*, 2007, pp. 1–8.
- [89] D. Martin, C. Fowlkes, D. Tal, and J. Malik, "A database of human segmented natural images and its application to evaluating segmentation algorithms and measuring ecological statistics," in *IEEE ICCV*, vol. 2, 2001, pp. 416–423.
- [90] C. Xia, J. Li, X. Chen, A. Zheng, and Y. Zhang, "What is and what is not a salient object? learning salient object detector by ensembling linear exemplar regressors," in *IEEE CVPR*, 2017.
- [91] Q. Yan, L. Xu, J. Shi, and J. Jia, "Hierarchical saliency detection," in *IEEE CVPR*, 2013, pp. 1155–1162.
- [92] Y. Li, X. Hou, C. Koch, J. M. Rehg, and A. L. Yuille, "The secrets of salient object segmentation," in *CVPR*, 2014, pp. 280–287.
- [93] B. W. Tatler, R. J. Baddeley, and I. D. Gilchrist, "Visual correlates of fixation selection: Effects of scale and time," *Vision research*, vol. 45, no. 5, pp. 643–659, 2005.
- [94] E. L. Kaufman, M. W. Lord, T. W. Reese, and J. Volkman, "The discrimination of visual number," *The American Journal of Psychology*, vol. 62, no. 4, pp. 498–525, 1949.
- [95] N. Otsu, "A threshold selection method from gray-level histograms," *IEEE transactions on systems, man, and cybernetics*, vol. 9, no. 1, pp. 62–66, 1979.
- [96] L. Breiman, *Classification and regression trees*. Routledge, 2017.
- [97] L.-C. Chen, G. Papandreou, I. Kokkinos, K. Murphy, and A. L. Yuille, "Deeplab: Semantic image segmentation with deep convolutional nets, atrous convolution, and fully connected crfs," *IEEE TPAMI*, vol. 40, no. 4, pp. 834–848, 2018.
- [98] K. He, X. Zhang, S. Ren, and J. Sun, "Deep residual learning for image recognition," in *IEEE CVPR*, 2016, pp. 770–778.
- [99] L. Bottou, "Stochastic gradient descent tricks," in *Neural networks: Tricks of the trade*. Springer, 2012, pp. 421–436.
- [100] F. Perazzi, P. Krähenbühl, Y. Pritch, and A. Hornung, "Saliency filters: Contrast based filtering for salient region detection," in *IEEE CVPR*, 2012, pp. 733–740.
- [101] D. Tsai, M. Flagg, and J. Rehg, "Motion coherent tracking with multi-label mrf optimization, algorithms," in *BMVC*, 2010.
- [102] P. Zhang, D. Wang, H. Lu, H. Wang, and X. Ruan, "Amulet: Aggregating multi-level convolutional features for salient object detection," in *IEEE ICCV*, 2017.
- [103] X. Yang, T. Mei, Y.-Q. Xu, Y. Rui, and S. Li, "Automatic generation of visual-textual presentation layout," *ACM Transactions on Multimedia Computing, Communications, and Applications (TOMM)*, vol. 12, no. 2, p. 33, 2016.
- [104] A. Jahanian, J. Liu, Q. Lin, D. Tretter, E. O'Brien-Strain, S. C. Lee, N. Lyons, and J. Allebach, "Recommendation system for automatic design of magazine covers," in *Proceedings of the 2013 international conference on Intelligent user interfaces*. ACM, 2013, pp. 95–106.
- [105] M. Sandler, A. Howard, M. Zhu, A. Zhmoginov, and L.-C. Chen, "Mobilenetv2: Inverted residuals and linear bottlenecks," in *CVPR*, 2018, pp. 4510–4520.
- [106] S. Mehta, M. Rastegari, L. Shapiro, and H. Hajishirzi, "Espnetv2: A light-weight, power efficient, and general purpose convolutional neural network," *CVPR*, 2019.
- [107] G.-Y. Nie, M.-M. Cheng, Y. Liu, Z. Liang, D.-P. Fan, Y. Liu, and Y. Wang, "Multi-level context ultra-aggregation for stereo matching," in *IEEE CVPR*, 2019.



Deng-Ping Fan received his PhD degree from Nankai University of Tianjin in 2019. He joined Inception Institute of Artificial Intelligence (IIAI), UAE in 2019. From 2015 to 2019, he was a Ph.D. candidate in Department of Computer Science, University of Nankai, directed by Prof. Ming-Ming Cheng. He received the Huawei Scholarship in 2017. His current research interests include computer vision, image processing and deep learning.



Ming-Ming Cheng received his PhD degree from Tsinghua University in 2012. Then he did 2 years research fellow, with Prof. Philip Torr in Oxford. He is now a professor at Nankai University, leading the Media Computing Lab. His research interests include computer graphics, computer vision, and image processing. He received research awards including ACM China Rising Star Award, IBM Global SUR Award, CCF-Intel Young Faculty Researcher Program, *etc.*



Zheng Lin is currently a Ph.D. candidate with College of Computer Science, Nankai University, under the supervision of Prof. Ming-Ming Cheng. His research interests include deep learning, computer graphics and computer vision.



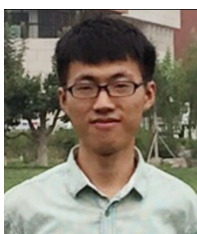
Jia-Xing Zhao is a master student at CCCE&CS, Nankai University (Tianjin, China). His advisor is Professor Ming-Ming Cheng. He received bachelor degree from Nankai University in 2017. His research interest includes computer vision and machine learning (especially deep learning).



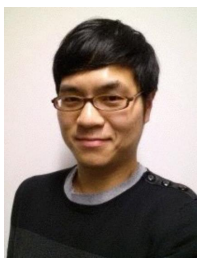
Yun Liu is a Ph.D. candidate with College of Computer Science and Control Engineering, Nankai University. He received his bachelor degree from Nankai University in 2016. His research interest includes computer vision and machine learning.



Zhao Zhang received the B.Eng degree from Yangzhou University in 2019. Currently, he is a master student in Nankai University under the supervision of Prof. Ming-Ming Cheng. His research interests includes computer vision and image processing.



Qibin Hou is currently a Ph.D. Candidate with College of Computer Science, Nankai University, under the supervision of Prof. Ming-Ming Cheng. His research interests include deep learning, image processing, and computer vision.



Menglong Zhu is a Computer Vision Software Engineer at Google. He obtained a Bachelors degree in Computer Science from Fudan University, in 2010, and a Masters degree in Robotics and a PhD degree in Computer and Information Science from University of Pennsylvania, in 2012 and 2016, respectively. His research interests are on object recognition, 3D object/human pose estimation, human action recognition, visual SLAM and text recognition.